Correlated domain structure in perovskite oxide superlattices exhibiting spin-flop coupling

Fan Yang, Nihan Kemik, Andreas Scholl, Andrew Doran, Anthony T. Young, Michael D. Biegalski, Hans M. Christen, and Yayoi Takamura

Phys. Rev. B **83**, 014417 — Published 19 January 2011

DOI: 10.1103/PhysRevB.83.014417

Correlated Domain Structure in Perovskite Oxide Superlattices Exhibiting Spin-Flop Coupling

Fan Yang[1], Nihan Kemik[1], Andreas Scholl[2], Andrew Doran[2], Anthony T. Young[2], Michael D. Biegalski[3], Hans M. Christen[3], and Yayoi Takamura[1,*]

[1] Department of Chemical Engineering and Materials Science, University of California, Davis, Davis, CA, 95616,

[2] Advanced Light Source, Lawrence Berkeley National Laboratory, Berkeley, CA 94720,

[3]Center for Nanophase Materials Science, Oak Ridge National Laboratory, Oak Ridge, TN 97831

RECEIPT DATE:

*To whom correspondence should be addressed: ytakamura@ucdavis.edu.

ABSTRACT:

We synthesized epitaxial perovskite oxide superlattices consisting of alternating ferromagnetic and antiferromagnetic sublayers with six unit cell sublayer thickness. This sublayer thickness corresponds to the maximum in interfacial spin-flop coupling for this system. Soft x-ray photoemission electron microscopy was used to observe the temperature dependence of the correlation between the ferromagnetic and antiferromagnetic domain structure in each sublayer. We confirm the local perpendicular alignment between the ferromagnetic and antiferromagnet moments and find that the strength of the spin-flop coupling dominates over the pinning effect of the structural domains which typically define the location of the antiferromagnetic domains.

PACS numbers: 75.70.Cn, 75.60.Ch, 75.25.-j

Multiferroic materials with multiple order parameters exist as promising candidate materials for stimulus-sensitive applications such as sensing, energy conversion, and information technology.[1] One approach involves finding a single material which displays these multiple order parameters, while a second approach involves the growth of epitaxial superlattices consisting of intimately coupled sublayers with their own functionality. A few remarkable examples have shown that interfaces of the perovskite oxides (ABO_3) can possess additional order parameters (i.e. superconductivity or ferromagnetism) despite the fact that they do not exist in the constituent materials.[2-4] Recently we showed that in all perovskite oxide superlattices consisting of alternating layers of the ferromagnetic (FM) metal, $La_{0.7}Sr_{0.3}MnO_3$ (LSMO) and the antiferromagnetic (AF) insulator $La_{0.7}Sr_{0.3}FeO_3$ (LSFO), a delicate balance exists between short-range electronic effects, long range (dipole) interactions and magnetic anisotropy.[5] For a sublayer thickness of six unit cells (~2.4 nm), we obtain a system where the LSMO sublayer remains FM, but the anisotropy of the LSFO layer has weakened sufficiently such that the direction of the AF spin axis can be reoriented by an applied magnetic field, mediated by a spin-flop coupling with the adjacent FM layers.[6-9] This behavior is in contrast to previous reports of exchange bias in the $LaFeO_3$/Co (AF oxide/FM metal) system where the anisotropy of the thick $LaFeO_3$ layer is able to pin the adjacent Co layer, causing a horizontal shift of the magnetic hysteresis loops.[10-11] This exchange bias lies at the heart of many magnetic devices used in magnetic recording read heads and magnetic random access memory devices, while device applications for spin-flop coupling remains largely unexplored. In the present study, soft-x-ray photoemission electron microscopy (PEEM) is used to observe the temperature dependence of the correlation between the FM and AF domain structure in our isostructural LSFO/LSMO superlattices. We find that the strength of the spin-flop coupling dominates over the ferromagnetic and antiferromagnetic properties of the individual layers and is able to overcome the pinning effect of the structural domains which typically define the location of the AF domains.

$La_{1-x}Sr_xMnO_3$ is a promising electrode material for information technology applications due to its wide range of interesting magnetic, electrical, and optical properties.[12] In particular, with a Sr doping level, x~0.33, it exhibits colossal magnetoresistance, a high degree of spin polarization, and coincident

metal/insulator and FM/paramagnetic transitions.[13] Meanwhile, $La_{1-x}Sr_xFeO_3$ is a G-type antiferromagnetic insulator in which the AF spin axis, $\boldsymbol{M_{Fe}}$, lies along the crystallographic ***a***-axis.[14] A uniform Sr doping level, x~0.33, leads to nearly equal Curie and Néel temperatures (T_C~T_N~ 360K) in the FM and AF bulk materials,[15-16] respectively and prevents Sr diffusion between the layers. The isostructural system permits the growth of superlattices with atomically sharp interfaces, without the occurrence of any oxidation or reduction reactions which may lead to uncompensated spins. The differing B site elements allows us to independently probe the FM and AF properties using x-ray absorption (XA) spectroscopy by tuning to the Mn or Fe absorption edges, respectively. Therefore, this system represents an ideal model system for investigating the interfacial coupling between FM and AF perovskite layers.

Epitaxial LSFO/LSMO superlattices consisting of six unit cells of LSFO and six unit cells of LSMO, repeated 10 times (referred to as [6 x 6]10) were grown on (001)-oriented single crystal $SrTiO_3$ (STO) substrates by pulsed laser deposition (PLD). For the deposition, a KrF laser (248 nm) at 10 Hz and a fluence of ~1.2 J/cm^2 was used and the substrate temperature was held at 700 ºC while the oxygen pressure was 200 mTorr. *In situ* reflection high energy electron diffraction was used to monitor the growth rate and to verify the layer-by-layer growth mode. After deposition, the superlattices were cooled slowly to room temperature in an oxygen pressure of 300 Torr to ensure the proper oxygenation of the films. The LSMO layer was grown first, so that the LSFO layer lies at the surface of the superlattice. High-resolution x-ray diffraction measurements confirm that the superlattices possess a high degree of crystallinity with the desired periodicity and smooth interfaces. Furthermore, reciprocal space maps (not shown) around the substrate 103, 301 and 331 reflections show that the films are fully coherent to the underlying STO substrate.

In the absence of uncompensated spins, a smooth interface between FM LSMO and G-type AF LSFO possesses an equal number of positive and negative exchange interactions such that no net exchange interaction should exist. However, using a microscopic Heisenberg model it is predicted that in this situation, the energy of the system will be minimized with a *perpendicular* coupling between the FM and AF moments, a phenomenon termed spin-flop coupling.[6-8] We previously confirmed the existence of

this spin-flop coupling in our [6x6]10 superlattice using soft x-ray magnetic spectroscopy measurements.[9] Furthermore, the alignment of the FM moments by an in-plane magnetic field has been shown to cause the reorientation of the AF moments in order to maintain this perpendicular orientation. The [6x6]10 superlattice was characterized by a suppressed saturation magnetization and T_C ~150 - 200 K for the LSMO sublayers and an enhanced T_N > 400 K for the LSFO sublayers. **Figure 1(a)** plots the magnetic hysteresis loops taken at 50 K using Mn x-ray magnetic circular dichroism (XMCD) with the magnetic field, $\boldsymbol{H_a}$, applied along the <100> and <110> substrate directions. These hysteresis loops possess two characteristics that distinguish them from those typically seen on LSMO films grown on STO substrates under a small tensile strain. Firstly, the coercive field, $\boldsymbol{H_C}$, is increased significantly to ~0.085 T compared to 0.005 T for single layer LSMO films. This increase in $\boldsymbol{H_C}$ is commonly observed in films which exhibit exchange bias. Secondly, the remnant magnetization is slightly higher along the <100> direction over the <110> direction, indicating this direction is the easy magnetization direction, unlike single layer LSMO films grown on (001)-oriented STO substrates where the magnetic easy axis typically lies along the <110> direction.[17]

PEEM images were obtained using the PEEM-3 microscope located on Beamline 11.0.1 at the Advanced Light Source. Using either circularly or linearly polarized x-rays, this technique provides images of the FM or AF domain structure, respectively, with high spatial resolution, elemental and chemical specificity as well surface sensitivity. The FM domain contrast arises due to XMCD in which the XA spectrum depends on the relative alignment of the local magnetization and the helicity of the circularly polarized x-rays. Images are captured using right and left circularly polarized (rcp/lcp) x-rays at a photon energy near the Mn L_3 absorption edge corresponding to the peak in the XMCD signal for LSMO. Because the magnetic contrast is opposite in images taken with rcp vs. lcp x-rays while the topography remains unchanged, the ratio of rcp and lcp images corresponds to a domain image without the topographic information. Domains that appear as bright/dark possess magnetizations which are parallel/antiparallel to the x-ray helicity, while gray domains have magnetizations which are perpendicular to the x-ray helicity. On the other hand, the AF domain contrast arises due to x-ray

magnetic linear dichroism (XMLD) where the XA spectrum differs depending on the angle between the x-ray polarization vector, $\boldsymbol{E}$ and $\boldsymbol{M_{Fe}}$.[18-19] In the PEEM-3 microscope, the x-rays are incident upon the sample at an angle, $\theta = 30°$ relative to the sample surface and along the *x*-axis (see schematic in **Fig. 1(b)**). $\boldsymbol{E}$ can be rotated between p-polarization (polarized parallel to the scattering plane) and s-polarization (polarized perpendicular to the scattering plane). The rotation angle of $\boldsymbol{E}$, denoted as β, is measured relative to p-polarization, such that for $\beta = 0°$, $\boldsymbol{E}$ cants out-of-plane making a 60° angle relative to the sample surface while for $\beta = 90°$, $\boldsymbol{E}$ lies completely in-the-plane of the sample along the *y*-axis. The angle between the scattering plane and the [100] direction of the sample is denoted by the angle ϕ. Domain images correspond to the ratio of images taken at the A and B peaks of the Fe L_2 absorption edge where the XMLD effect is maximized. The polarization dependence of the intensity at the Fe $L_{3,2}$ absorption edges is given by: $I(\alpha) = a + b\left(3\cos^2\alpha - 1\right)\left\langle M^2\right\rangle_T$ where *a* and *b* are constants, α is the angle between $\boldsymbol{E}$ and $\boldsymbol{M_{Fe}}$, and $\left\langle M^2\right\rangle_T$ is the square of the AF moment.

The AF domain images taken at *T*~38 K for the [6x6]10 superlattice are shown in **Figure 2** for ϕ = 10° and -35°. All images are shown with the same contrast conditions. As $\boldsymbol{E}$ varies from out-of-plane ($\beta = 0°$) to in-plane ($\beta = 90°$), two distinct types of domain can be identified. For $\phi = -35°$, the strongest contrast between the two domains occurs for $\beta \sim 60°$, while for $\phi = 10°$, the strongest contrast occurs for $\beta \sim 80°$, indicating that the spin axis, $\boldsymbol{M_{Fe}}$ within these domains are almost parallel/perpendicular to the $\boldsymbol{E}$ vector under these conditions. Quantitative analysis of the local intensity for each type of domain (symbols in Figure 3(c) and (d)) was extracted from the images and then normalized to the average intensity for the entire ratio image. This procedure removes an artificial modulation of the experimental, angular dependent XMLD curves because of small changes in the image illumination and x-ray intensity with changes in polarization and energy. This non-magnetic artifact has equal amplitude in both types of domains and it is easily removed by the normalization to the average intensity. Error values represent the sigma value for the Gaussian curves used to fit the experimental data.

These values are compared to a two domain model where $\boldsymbol{M_{Fe}}$ lies in-plane along the <100> family of directions (solid lines in Figure 3(c) and (d)). This model also incorporates the orientation of the sample relative to the x-ray beam (i.e. 30º incidence angle and ϕ angle). The curves were divided by their average value to facilitate the comparison with the normalized experimental data. Good agreement exists with the model contrast level in regards to the trends and most importantly the locations of the crossing points. These crossing points are unchanged in polarization angle regardless of the analysis procedure (with and without the normalization to the average value) and they are highly sensitive to the ϕ angle, and thus they serve as key indicators to match the experimental data to the model. Polarization rotation series taken as a function of temperature reveal that the direction of $\boldsymbol{M_{Fe}}$ remains unchanged up to room temperature, i.e. above the T_C of the LSMO sublayers, however, the locations of the AF domains change with temperature. It should be noted that no FM domain contrast was observed on the Fe absorption edge, indicating the absence of uncompensated Fe spins in the LSFO layer.

Figure 3 compares the Fe XMLD (β = 90°, first column) and Mn XMCD (second column) domain images at ~ 57 K for two sample orientations relative to the x-ray beam, ϕ = 10º and -35º. These images were taken under zero applied magnetic field conditions with a demagnetized sample. We will show that the type of AF domain in the LSFO sublayer directly impacts the type of FM domains that form in the adjacent LSMO sublayers. Specifically, within a given micrometer-sized AF domain, only two types of smaller (~200 nm wide) FM domains such that locally the perpendicular orientation between $\boldsymbol{M_{Fe}}$ and $\boldsymbol{M_{Mn}}$ expected from the spin-flop coupling is maintained. From the analysis of the AF domain contrast above, we know that with ϕ = 10º and β = 90º, $\boldsymbol{M_{Fe}}$ within the white/black domains lies at angles of 10º/100º relative to the x-ray $\boldsymbol{E}$ vector, while for ϕ = -35º, $\boldsymbol{M_{Fe}}$ lies at angles of -35º/55º. Considering the first pair of images for ϕ = 10º where the AF domains are predominantly black, the Mn XMCD images show the formation of many small, irregularly shaped FM domains with strong white/black contrast, corresponding to regions where $\boldsymbol{M_{Mn}}$ is *parallel/antiparallel* (190º/10º) to the x-ray helicity (*x*-axis). Upon close inspection we notice that the white/black regions are occasionally separated

by small gray regions (highlighted by (green) lines in Figure 3). No clear boundaries can be observed between the gray and white/black regions as the domain wall width lies below the spatial resolution of the microscope. This gray (intermediate) contrast indicates a *perpendicular* (-80º/100º) alignment between $\boldsymbol{M_{Mn}}$ and the x-ray helicity (i.e. $\boldsymbol{M_{Mn}}$ nearly parallel/antiparallel to the *y*-axis). Most importantly, a comparison to the Fe XMLD image shows that these gray regions correspond directly to the white AF domains ($\boldsymbol{M_{Fe}}$ almost perpendicular to $\boldsymbol{E}$ and the *y*-axis). Similarly, the black AF domains ($\boldsymbol{M_{Fe}}$ almost parallel to $\boldsymbol{E}$ and the *y*-axis) correspond to the regions with the strong white/black contrast (i.e. $\boldsymbol{M_{Mn}}$ nearly perpendicular to the *y*-axis). For comparison, a second region of the sample with predominantly white AF domains is shown at lower magnification in the second pair of images in the third and fourth columns of Fig. 3(a). Fig. 3(c) compares line profiles taken across a series of black/white AF domains and the corresponding line profile in the Mn XMCD image. The black AF domains correspond to regions in the Mn XMCD with two colors (white/black), while the contrast is uniformly gray within the white AF domains. Therefore, these images confirm the *perpendicular* alignment of the Fe and Mn moments in the adjacent sublayers as shown schematically in Fig. 1(c). Further confirmation can be obtained by examining the images for ϕ = -35º (Figure 3(b)). The Mn XMCD images show regions with strong white/black contrast separated by regions with weaker light gray/dark gray contrast. Due to the reduced contrast difference between the domains, it is more difficult to clearly distinguish between regions, however these regions with light gray/dark gray contrast almost appear as being "blurry" despite the fact that the single images remain in focus throughout the image. It should be noted that at ϕ = -45º, $\boldsymbol{M_{Mn}}$ of all four types of domains would lie at angles of -45º/135º/45º/225º relative to the x-ray helicity and therefore they would be indistinguishable from one another. By carefully comparing the Fe XMLD and Mn XMCD images, we find that a correlation exists between the AF and FM domains. Within the black AF domains ($\boldsymbol{M_{Fe}}$ at an angle of -35º from the *y*-axis), two types of small FM domains are observed with strong white/black contrast ($\boldsymbol{M_{Mn}}$ at -35º/145º relative to the x-ray helicity or 55º/235º to the *y*-axis). The relative contrast for the FM domains within the white AF domains ($\boldsymbol{M_{Fe}}$ at an angle of 55º from the *y*-axis) is reduced as $\boldsymbol{M_{Mn}}$ forms angles of 55º/235º (closer to perpendicular) to the x-ray helicity (-35º/145º

to the *y*-axis). Quantitative analysis of the local intensity of the FM domains follows the expected cosine dependence between $\boldsymbol{M_M}$ and the x-ray helicity. Based on the results shown in Figures 2 and 3, we can conclude that $\boldsymbol{M_{Fe}}$ within the AF domains lies along the in-plane <100> directions, and the Mn magnetization within the FM domains orients along the <100> substrate directions such that a perpendicular alignment is maintained between the Mn and Fe moments. This orientation of the Mn magnetization is in agreement with the XMCD hysteresis loops which show that the <100> direction is the magnetic easy direction.

The perpendicular coupling remains unchanged for increasing temperature up to the T_C of the LSMO sublayer ~ 160 K when the Mn XMCD domain contrast disappears. However, as shown in **Figure 4**, the locations of the AF domains, and consequently the FM domains change with increasing temperature. Moreover, at low temperatures (below ~ 100K) the AF domains are observed to arrange into elongated stripes, tens of microns in width, of primarily white or black domains with the edges of the stripes aligned approximately along the in-plane <110> substrate directions. The edges of these stripes are outlined in Figures 2-4, though they are more apparent in the low magnification image shown in Figure 2. In contrast, at room temperature the white and black domains are uniformly distributed in the LSFO layers. This movement of the domains implies that for a given location, the Fe and Mn spins make 90º and/or 180º rotations upon changes in temperature. Temperature dependent domain imaging have shown that the FM domains in LSMO/non-magnetic $La_{0.5}Sr_{0.5}TiO_3$ superlattices (not shown) and $La_{0.65}Ca_{0.35}MnO_3$ thin films also show 90º spin rotations upon changes in temperature near the T_C.[20] In contrast, this behavior is unlike that of single layer $LaFeO_3$ (LFO) films where the location of the AF domains have been shown to correspond to structural twins in the films[10] and therefore remain in fixed locations with increasing temperature.[21] Therefore, using temperature dependent PEEM imaging and magnetic spectroscopy, we find that the strength of the spin-flop coupling dominates over the weakened anisotropy of the LSFO sublayers in the [6x6]10 superlattice such that the structural domains no longer pin the locations of the AF domains.

In summary, our previous soft x-ray magnetic spectroscopy measurements revealed that in a [6x6]10 superlattice the application of an in-plane magnetic field results in the reorientation of the AF spin axis due to the spin-flop coupling with the adjacent FM LSMO layers.[9] In this work, we investigated the correlation between the AF and FM domains as a function of temperature in this isostructural superlattice system using photoemission electron microscopy. These images confirm the perpendicular alignment between the AF spin axis and the Mn magnetization such that each micrometer-sized AF domain corresponds to two types of smaller (~200 nm wide) FM domains. The locations of the AF and FM domains move together with changes in temperature up to the T_C of the LSMO layer (~ 160 K), proving that the strength of the spin-flop coupling can overcome the anisotropy of LSFO and the pinning effect of the structural domains which typically define the location of AF domains in thicker layers. Furthermore, the orientation of the Mn easy axis lies along the <100> directions, differing from what is typically observed in LSMO films grown under tensile strain on (001)-oriented STO substrates. Therefore, the robust spin-flop coupling observed in the [6x6]10 superlattice dominates over the ferromagnetic and antiferromagnetic properties of the individual layers, and it has the potential to lead to the development of device designs which harness the ability to reorient the AF spin axis.

The authors thank Dr. A. Mehta and M. Bibee (SSRL) for assistance with acquiring the XRD data. Research at the ALS, CNMS and SSRL is supported by the Division of Scientific User Facilities, Office of Basic Energy Sciences, U.S. Department of Energy. Research at UC Davis is supported by UC Davis start-up funds and the National Science Foundation Contract No. DMR 0747896.

Figure captions:

FIGURE 1: (Color online) (a) XMCD hysteresis loops taken at 50K for the [6x6]10 superlattice with the magnetic field applied in-plane along the <100> and <110> substrate directions, (b) schematic of the PEEM-3 microscope, $\boldsymbol{M_{Fe}}$ in the AF domain and $\boldsymbol{M_{Mn}}$ in the FM domains relative to the x-ray scattering plane for two sample orientations, (c) ϕ = 10º and (d) ϕ = -35º.

FIGURE 2: (Color online)AF domain images taken at T~ 38K with varying β for (a) ϕ = 10° and (b) ϕ = -35°; (c) and (d) experimental contrast vs. β obtained from images in (a) and (b) and calculated contrast for a two domain model with the $\boldsymbol{M_{Fe}}$ lying in-plane along the <100> directions. The (green) lines in (a) and (b) highlight the edges of a white/black stripe in the AF domain pattern.

FIGURE 3: (Color online) AF (with β = 90°) and FM domain images for (a) ϕ = 10º and (b) ϕ = -35º. The (green) lines outline the locations of a few AF domains. Two locations with predominantly black or white AF domains for the case of ϕ = 10º are shown. The second pair of images is taken at lower magnification to give a better overview of the correlation between images. (c) Line profiles taken across a set of black/white/black AF domains and the corresponding line profile from the Mn XMCD image. The path is indicated by the (blue) lines in the domain images. Vertical lines are guides to the eye to denote the boundary between AF domains while the horizontal bar denotes the region defined as gray in the Mn XMCD image.

FIGURE 4: (Color online) (a) AF (with β = 90º) and (b) FM domain images as a function of temperature for ϕ = 10º. The (green) lines outline the locations of a few AF domains and the edge of a white/black stripe seen at temperature below ~100K.

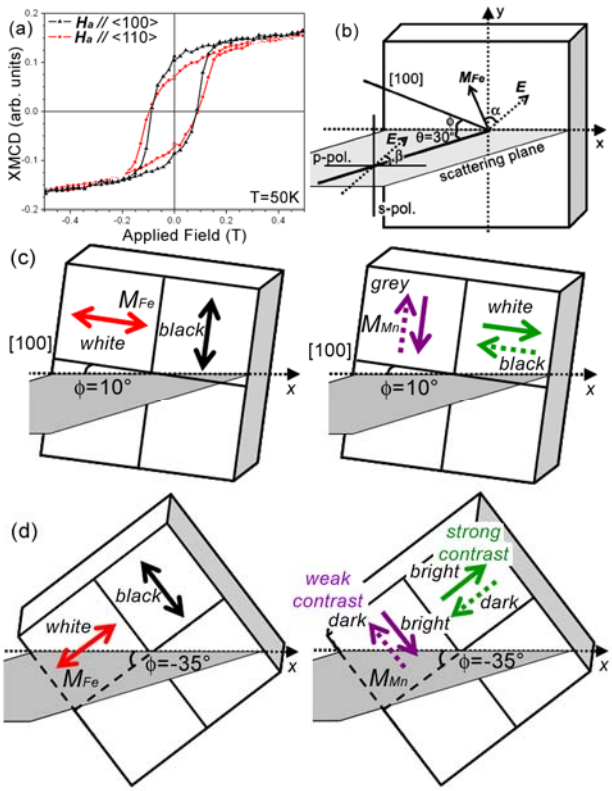
(a)
H_a // <100>
H_a // <110>
XMCD (arb. units)
T=50K
Applied Field (T)
(b)
y
[100]
M_{Fe}
E
α
θ=30°
β
x
p-pol.
s-pol.
scattering plane
(c)
M_{Fe}
white
black
[100]
ϕ=10°
x
grey
M_{Mn}
white
black
[100]
ϕ=10°
x
(d)
black
white
M_{Fe}
ϕ=-35°
x
strong
contrast
bright
dark
weak
contrast
dark
bright
M_{Mn}
ϕ=-35°
x

Figure 1

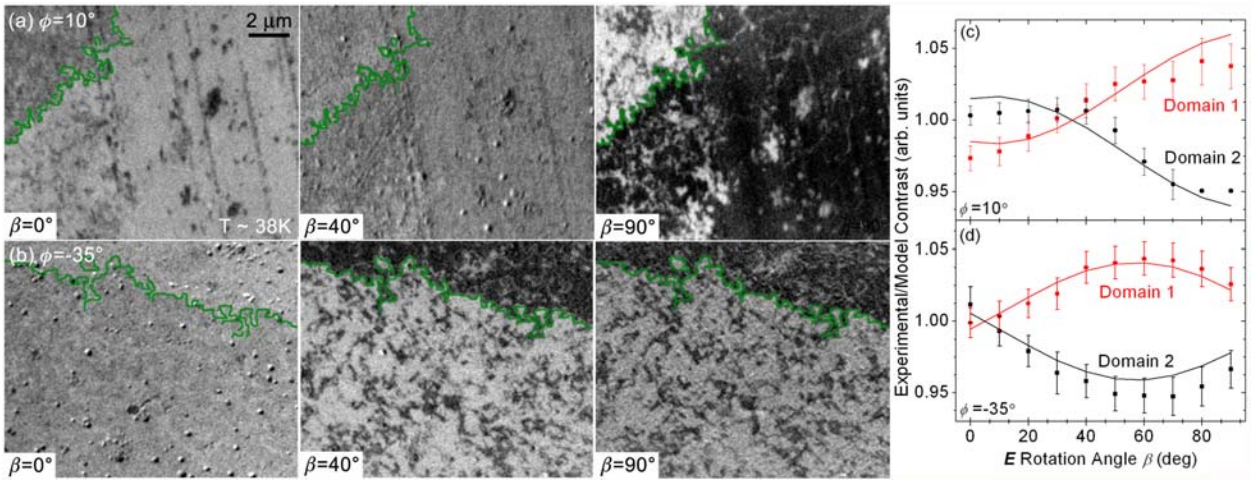
(a) φ=10°
2 μm
β=0°
T ~ 38K
β=40°
β=90°
(b) φ=-35°
β=0°
β=40°
β=90°
(c)
Domain 1
Domain 2
φ =10°
(d)
Domain 1
Domain 2
φ =-35°
Experimental/Model Contrast (arb. units)
1.05
1.00
0.95
0
20
40
60
80
E Rotation Angle β (deg)

Figure 2:

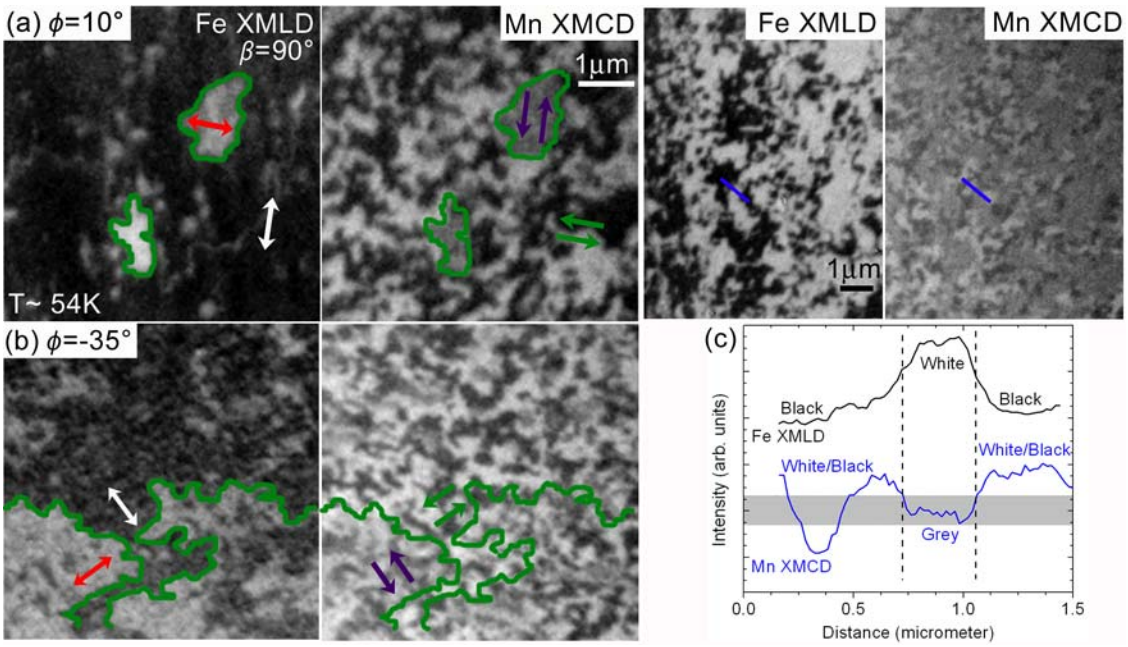
(a) ϕ=10°
Fe XMLD
β=90°
Mn XMCD
1μm
Fe XMLD
Mn XMCD
1μm
T~ 54K
(b) ϕ=-35°
(c)
White
Black
Black
Fe XMLD
White/Black
White/Black
Grey
Mn XMCD
Intensity (arb. units)
0.0
0.5
1.0
1.5
Distance (micrometer)

Figure 3:

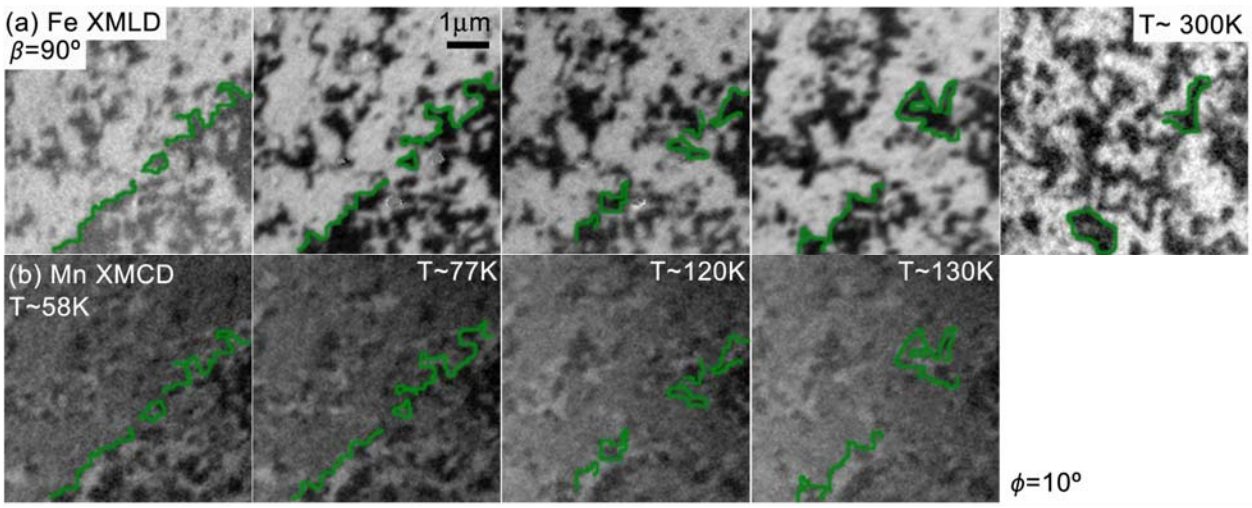

Figure 4:

References

1. R. Ramesh and N. A. Spaldin, Nat. Mater. **6**, 21-29 (2006).
2. A. Ohtomo and H. Y. Hwang, Nature **427**, 423-426 (2004).
3. R. Pentcheva and W. E. Pickett, Phys. Rev. B **74**, 035112 (2006).
4. N. Reyren, S. Thiel, A. D. Caviglia, L. Fitting Kourkoutis, G. Hammerl, C. Richter, C. W. Schneider, T. Kopp, A.-S. Ruetschi, D. Jaccard, M. Gabay, D. A. Muller, J.-M. Triscone and J. Mannhart, Science **317**, 1196-1199 (2007).
5. Y. Takamura, F. Yang, N. Kemik, E. Arenholz, M. D. Biegalski and H. M. Christen, Phys. Rev. B **80** (180417(R)) (2009).
6. L. L. Hinchey and D. L. Mills, Phys. Rev. B **34** (3), 1689-1699 (1986).
7. N. C. Koon, Phys. Rev. Lett. **78** (25), 4865-4868 (1997).
8. T. C. Schulthess and W. H. Butler, Phys. Rev. Lett. **81** (20), 4516-4519 (1998).
9. E. Arenholz, G. van der Laan, F. Yang, N. Kemik, M. D. Biegalski, H. M. Christen and Y. Takamura, Appl. Phys. Lett. **94**, 072503 (2009).
10. J. W. Seo, E. E. Fullerton, F. Nolting, A. Scholl, J. Fompeyrine and J.-P. Locquet, J. Phys.- Condens. Mat. **20**, 264014 (2008).
11. F. Nolting, A. Scholl, J. Stohr, J. W. Seo, J. Fompeyrine, H. Siegwart, J.-P. Locquet, S. Anders, J. Luning, E. E. Fullerton, M. F. Toney, M. R. Scheinfein and H. A. Padmore, Nature **405**, 767-769 (2000).
12. Y. Tokura and N. Nagaosa, Science **288**, 462-468 (2000).
13. A. P. Ramirez, J. Phys-Condens Mat **9**, 8171-8199 (1997).
14. R. L. White, J. Appl. Phys. **40** (3), 1061-1069 (1969).
15. J.-C. Grenier, N. Ea, M. Pouchard and M. Abou-Sekkina, Mater. Res. Bull. **19**, 1301-1309 (1984).
16. U. Shimony and J. M. Knudsen, Phys. Rev. **144** (1), 361-366 (1966).
17. L. M. Berndt, V. Balbarin and Y. Suzuki, Appl. Phys. Lett. **77** (18), 2903-2905 (2000).

18. D. Alders, L. H. Tjeng, F. C. Voogt, T. Hibma, G. A. Sawatzky, C. T. Chen, J. Vogel, M. Sacchi and S. Iacobucci, Phys. Rev. B **57** (18), 11623-11631 (1998).
19. P. Kuiper, B. G. Searle, P. Rudolf, L. H. Tjeng and C. T. Chen, Phys. Rev. Lett. **70** (10), 1549-1552 (1993).
20. Q. Lu, C.-C. Chen and A. De Lozanne, Science **276**, 2006-2008 (1997).
21. A. Scholl, J. Stohr, J. Luning, J. W. Seo, J. Fompeyrine, H. Siegwart, J.-P. Locquet, F. Nolting, S. Anders, E. E. Fullerton, M. R. Scheinfein and H. A. Padmore, Science **287**, 1014-1016 (2000).